Strong interaction and mass measurements using antiprotonic atoms*

P. Roberson,[†] T. King,[‡] and R. Kunselman
University of Wyoming, Laramie, Wyoming 82071

J. Miller[§] and R. J. Powers
California Institute of Technology, Pasadena, California 91125

P. D. Barnes, R. A. Eisenstein, and R. B. Sutton
Carnegie-Mellon University, Pittsburgh, Pennsylvania 15213

W. C. Lam[¶]
Virginia Polytechnic Institute and State University, Blacksburg, Virginia 24061

C. R. Cox,[‖] M. Eckhause, J. R. Kane, A. M. Rushton,[**] W. F. Vulcan, and R. E. Welsh
College of William and Mary, Williamsburg, Virginia 23185
(Received 2 May 1977)

X-ray transition energies of antiprotonic atoms formed in targets of ^{6}Li, ^{7}Li, C, Si, P, Fe, Y, Zr, Cs, and Yb have been measured. Level shifts and widths due to the strong interaction were determined. A phenomenological fit to the data using an optical-model potential proportional to the nuclear matter density and to an effective $\bar{p}$-nucleus s-wave scattering length yielded $[(0.85 \pm 0.38) + i(2.66 \pm 0.28)]$ fm for the effective scattering length. In addition, the mass of the antiproton was determined to be 938.229 ± 0.049 MeV from the observed energies of the $\bar{p}$ x-ray transitions unperturbed by the strong interaction.

> NUCLEAR REACTIONS, hadronic atoms. Measured antiprotonic atom x-ray transition energies; determined strong interaction shifts and widths; deduced effective scattering length; deduced antiproton mass.

I. INTRODUCTION

We have observed x rays from antiprotonic atoms formed by stopping antiprotons in target materials of ^{6}Li, ^{7}Li, C, Si, P, Fe, Y, Zr, Cs, and Yb. The antiprotons cascade through the atomic states until they are captured by the nucleons in the nucleus. The terminating x-ray transition places the antiproton in a level of principal quantum number n, from which the probability of nuclear absorption vastly dominates the probability of an electromagnetic transition. This transition will reflect observable effects on the energies, yields, and line widths due to the strong interaction. Antiprotons in the upper state of the terminating radiative transition are partially absorbed by the nucleus producing a reduction in the x-ray yield. The lower state may exhibit an experimentally observable broadening and a level shift due to the strong interaction. The energies of the transitions between levels with larger values of n are almost unaffected by the strong interaction and can be used to determine the antiproton mass.

Section II contains a discussion of the theory used to calculate the electromagnetic energy levels, the relative electromagnetic transition intensities, and the strong-interaction parameters.

Experimental details are presented in Sec. III, data reduction techniques in Sec. IV, and results and conclusions in Sec. V.

II. THEORETICAL CONSIDERATIONS

A. Energy level calculations

The Dirac equation describes a structureless particle of spin $\frac{1}{2}$ and magnetic moment $\mu_p = e\hbar/2mc$, where m is the mass of the particle. The resulting eigenvalues are[1]

$$E_{nj} = \mu c^2 \left[1 + \left(\frac{Z\alpha}{n - (j + \frac{1}{2}) + [(j + \frac{1}{2})^2 - (Z\alpha)^2]^{1/2}} \right)^2 \right]^{-1/2},$$

(1)

where μ is the reduced mass of the nucleus-particle system, n is the principal quantum number, j is the total angular momentum quantum number, Z is the charge of the nucleus, and $\alpha = e^2/\hbar c$ is the fine-structure constant. Only two quantum numbers n and j are necessary to specify the energy of a state because energy levels of different orbital quantum numbers l and the same n and j are degenerate in Dirac theory. This degeneracy is destroyed by the inclusion of various corrections to the energy levels.

In general, corrections must be included for nuclear finite-size effects, radiative corrections, interactions between the antiproton and higher moments of the nucleus, electron screening, and the anomalous magnetic moment of the antiproton. We shall summarize the approaches used in calculating these corrections. A more complete theoretical discussion appears in the review article on exotic atoms by Seki and Wiegand.[2] Table I is a list of typical corrected electromagnetic energies for several antiprotonic states. The estimated accuracy of these calculated corrections is of the order of 1 eV.

1. Vacuum polarization

We used the vacuum-polarization potentials derived by Blomqvist.[3] Terms of order $\alpha Z\alpha$ are large enough to require second-order perturbation theory. The contributing terms consist of the $\alpha Z\alpha$ potential squared and the cross term of the $\alpha Z\alpha$ potential with the finite-size correction potential.

In addition, there is a small contribution to the vacuum polarization from interference effects of the strong interaction potential in the terminating transition.

The calculations can also be carried out using μ^{+}-μ^{-} virtual pairs. Since the muon mass is larger than the electron mass, these processes do not constitute a significant correction.

2. Anomalous magnetic moment

Although the anomalous moment of the antiproton is large (compared to the normal moment), and cannot be accounted for by quantum electrodynamics alone, it can be treated adequately by first-order perturbation theory just as is the anomalous moment of the electron. According to Bethe and Salpeter[1] and Pilkuhn,[4] the perturbing energy is

$$\Delta E_{AM}(nlj) = -2g_1 \mu_p Ze^2 \int_0^\infty \frac{G_{lj}(r)F_{lj}(r)}{r^2} dr, \quad (2)$$

where $g_1 = 1.7928$ is the anomalous moment in units

TABLE I. Contributions to the calculated electromagnetic energies. VP is vacuum polarization. HO is higher order. AMM is anomalous magnetic moment. NP is nuclear polarization. FS is finite size. NM is nuclear motion. ES is electron screening. Column two lists several selected states, the lowest order and higher order vacuum polarizations are in columns four and five, and the anomalous magnetic moment correction, the nuclear polarization, the finite size nucleus, the nuclear motion, and the electron screening corrections are in columns six through ten. All energies are in eV.

Element	State	Dirac energy $(E_{nj} - \mu c^2)$	VP $\alpha Z\alpha$	HO	AMM	NP	FS	NM	ES	Total
^{6}Li	$2p_{3/2}$	−48 149	−168	−1	7	0	3	0	0	−48 308
	$3d_{5/2}$	−21 399	−36	0	1	0	0	0	0	−21 434
^{7}Li	$2p_{3/2}$	−49 155	−174	−1	7	0	4	0	0	−49 319
	$3d_{5/2}$	−21 846	−37	0	1	0	0	0	0	−21 882
^{nat}C	$3d_{5/2}$	−92 202	−300	−2	14	0	0	0	0	−92 490
	$4f_{7/2}$	−51 863	−101	−1	3	0	0	0	0	−51 962
^{nat}Si	$4f_{7/2}$	−295 486	−1 172	−7	99	0	0	−2	0	−296 568
	$5g_{9/2}$	−189 100	−539	−3	32	0	0	−1	0	−189 611
^{nat}P	$4f_{7/2}$	−340 312	−1 413	−9	131	−1	1	−2	0	−341 605
	$5g_{9/2}$	−217 785	−657	−4	42	0	0	−1	0	−218 405
^{nat}Fe	$5g_{9/2}$	−633 793	−2 938	−15	381	−4	1	−4	0	−666 372
	$6h_{11/2}$	−460 916	−1 598	−7	150	−1	0	−2	−1	−462 375
^{nat}Y	$6h_{11/2}$	−1 044 266	−4 732	−12	767	−8	2	−7	−1	−1 048 257
	$7i_{13/2}$	−767 101	−2 846	−5	350	−2	0	−4	−2	−769 610
^{nat}Zr	$6h_{11/2}$	−1 098 845	−5 054	−1	849	−9	2	−7	−1	−1 103 076
	$7i_{13/2}$	−807 188	−3 046	−5	388	−2	0	−4	−2	−809 859
^{nat}Cs	$7i_{13/2}$	−1 531 935	−7 086	16	1 393	−17	2	−9	−4	−1 537 640
	$8j_{15/2}$	−1 172 661	−4 579	16	707	−5	0	−6	−6	−1 176 534
^{174}Yb	$8j_{15/2}$	−1 903 638	−8 665	77	1 861	−22	1	−11	−13	−1 910 410
	$9k_{17/2}$	−1 503 787	−5 890	63	1 024	−8	0	−7	−19	−1 508 624

of the antiproton magneton, and G and F are the wave functions of a Dirac particle in a point Coulomb field. The resulting fine-structure (FS) splitting (including the normal spin moment splitting) is close to the nonrelativistic limit of

$$\Delta E_{\rm FS}(nl) = (1 + 2g_1)\frac{(Z\alpha)^4}{2n^3}\frac{\mu c^2}{l(l+1)}. \tag{3}$$

For the $n = 7$ to $n = 6$ transition in Y, the nonrelativistic formula gives a fine-structure splitting of 1.184 keV, while the relativistic formula gives 1.180 keV.

3. Nuclear polarization

We followed the treatment of Cole[5] in calculating the nuclear polarization correction. It is calculated in second-order perturbation theory with the giant dipole (GD) nuclear excitations dominating. The antiproton is absorbed from a high enough atomic level so that this correction never becomes large enough to require a detailed calculation. The energy shift is given by

$$\Delta E_{NP}(nlj) = -\frac{\alpha^2 NZ\hbar^4 c^2}{2AM}\frac{1}{E^2_{GD}}\langle nlj\,|\,1/r^4\,|\,nlj\rangle, \tag{4}$$

where $E^2_{\rm GD} \approx 770(NZ/M)(\hbar^2/A^{8/3})$ is the energy of the giant dipole resonance and M is the nucleon mass.[6]

4. Finite size

The finite-size correction accounts for the fact that the nuclear charge potential is not point Coulomb. The nuclear charge potential is determined from the charge distribution

$$\phi(r) = \int \frac{\rho(r')}{|r - r'|}d^3r'. \tag{5}$$

The energy correction is then

$$\Delta E_{\rm FS}(nlj) = \langle nlj\,|\,e\phi(r) - Ze^2/r\,|\,nlj\rangle. \tag{6}$$

5. Nuclear motion

The main effect of nuclear motion (NM) is taken into account by the use of the reduced mass in the Dirac equation. This prescription is exact only for the nonrelativistic case. There is a correction due to the change in kinetic energy and one due to the retardation of the electromagnetic potential. Blomqvist[3] gives an approximate formula for this correction, valid only for states in which the relativistic and finite-nuclear-size effects are small:

$$E_{\rm NM}(n) = -\frac{\mu^2(Z\alpha)^4}{8Mn^4}. \tag{7}$$

This formula is sufficiently accurate for all antiprotonic atomic states of interest.[7]

6. Electron screening

The density of the electronic wave functions inside the orbit of the antiproton decreases the net positive charge and affects the binding of the antiproton. The size of the electron screening correction is uncertain due to the uncertainty in the number of electrons present at any time (because of Auger transitions) and the unknown nature of the effect of the antiproton on the electron orbits. Vogel[8] has shown that a sufficient accuracy (3%) can be attained by using the electron configuration of the $(Z - 1)$ atom, and derives an empirical formula for the screening potential. This potential is valid only for $Z \gtrsim 30$. However, the extrapolation of the energy corrections to low-Z atoms agreed with an independent method of calculation,[9] and were sufficiently accurate for the relevant antiprotonic atomic states.

7. Hyperfine structure

For the antiprotonic transitions of interest for these measurements, only the electric quadrupole interaction ($E2$) was large enough to produce significant hyperfine structure (hfs), and only in ^{174}Yb. Chen et al.[10] developed a formula using nonrelativistic wave functions and perturbation theory in terms of the excitation energy ϵ of the first nuclear excited state and the transition and static intrinsic quadrupole moments q_{02} and q_{22}. In the case of the ^{174}Yb one has $\epsilon = 76.48$ keV and $q_0 = 7.83$ b.[11] The fine-structure averaged corrections to the state energies are $\Delta E(n = 8, l = 7) = -833$ eV, $\Delta E(11, 10) = -18$ eV. The quadrupole hyperfine structure of ^{91}Zr did not alter the $n = 7$ to $n = 6$ transition significantly.

B. Cascade

The antiproton is captured by a target nucleus into very high-n atomic states in the midst of the electron cloud. The initial capture distribution as a function on n and l is uncertain. The antiproton cascades by two competing processes: Auger and radiative transitions. If electrons are available to absorb the energy, Auger transitions dominate. Radiative transitions are important only for states well inside the electron cloud ($n \ll 42$).

Figure 1 gives a representative cascade in the region of radiative transition dominance. Only electric dipole transitions are significant. Also, the $(n, l) \to (n', l+1)$ transitions are much smaller in intensity than the $(n, l) \to (n', l - 1)$ transitions. The radiative transitions tend to enhance the populations of circular levels ($l = n - 1$) at the expense of the noncircular. This is due to the fact that radiative transitions are enhanced relative to
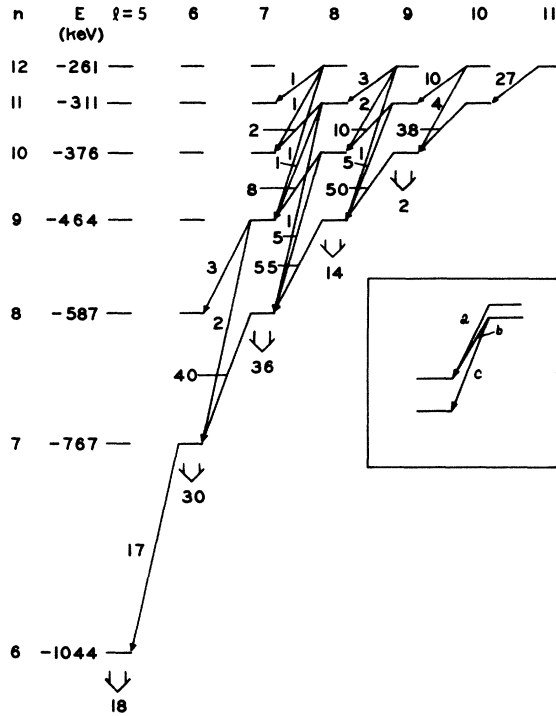
FIG. 1. The calculated cascade for Y. The large arrows represent nuclear absorption from all n levels for each l. The transition and absorption intensities represent percentages of all captured antiprotons. Each transition is actually a triplet and the fine structure is shown in the insert.

Auger for $\Delta n > 1$.

The width due to nuclear absorption from the state in which the terminating radiative transition originates ($n = 7, l = 6$ in Fig. 1) can be determined using the x-ray intensities. The relative yield Y is defined as the number of radiative transitions compared to the total number of transitions

$$Y = \frac{W_X}{W_x + W_A + W_a} , \qquad (8)$$

where W_X is the radiative transition rate, W_A is the Auger transition rate, and W_a is the nuclear absorption rate. For the observable transition with the lowest quantum number n the Auger rate is negligible. The nuclear absorption width of the upper level is then

$$\Gamma_{\text{upper}} = \hbar W_X (1/Y - 1) . \qquad (9)$$

The radiative rate is calculated using the correction for the motion of the nucleus about the center of mass of the antiproton-nucleus system.[12] The yield is determined from the data by dividing the intensity of the last observable transition by the sum of the intensities of all the transitions feeding the upper level, and correcting for the

detector efficiency.

Each transition of Fig. 1 is actually a triplet due to the fine-structure splitting, as shown in the insert. The relative intensities of the components depend on the statistical populations of the levels (except for a small effect due to the strong interaction absorption). For an $l \to l - 1$ transition, $a : b : c = (2l - 1)(l + 1) : 1 : (2l + 1)(l - 1)$. Note that the transitions are effectively only doublets for large l.

C. Strong interaction in antiprotonic atoms

We describe the strong interaction of the antiproton with the nucleus by a complex potential V_N. The assumption made in formulating V_N is that it is proportional to the density distribution of protons and neutrons in the nucleus, because the s-wave interaction dominates. If $V_N(r)$ is assumed to be of the form $C_1 \rho_n(r) + C_2 \rho_p(r)$, where ρ_n and ρ_p are the neutron and proton density distributions, normalized to N and Z, respectively, and C_1 and C_2 are constants, the average s-wave scattering length $\bar{a}$ per nucleon is

$$\bar{a} = -\frac{2\mu}{A\hbar^2} \left[C_1 \int_0^\infty \rho_n(r) r^2 dr \right.$$
$$\left. + C_2 \int_0^\infty \rho_p(r) r^2 dr \right] . \qquad (10)$$

The average s-wave scattering length can also be expressed in terms of single-nucleon scattering lengths as $\bar{a}\rho(r) = a_1 \rho_n(r) + \frac{1}{2}(a_0 + a_1)\rho_p(r)$, where $\rho(r)$ is the average matter-density distribution, normalized to A, and a_0 and a_1 are the single-particle scattering lengths for isospin channels 0 and 1, respectively.

From these relationships it can be shown that[2]

$$V_N(r) = -(4\pi\hbar^2/2\mu)[a_1\rho_n(r) + \frac{1}{2}(a_0 + a_1)\rho_p(r)]$$
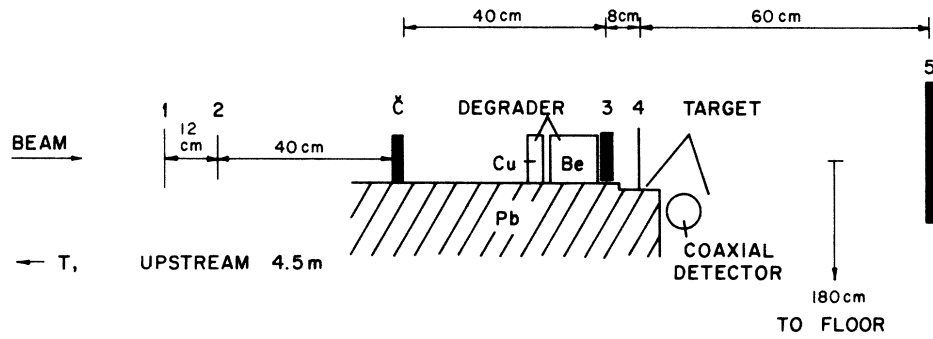$$\times (1 + m/M) \qquad (11)$$

or

$$V_N(r) = -(4\pi\hbar^2/2\mu)\bar{a}\rho(r)(1 + m/M) , \qquad (12)$$

where m is the $\bar{p}$ mass, M the nucleon mass, and where the last factor has been included in order to convert the free-nucleon scattering length to the bound-nucleon scattering length.

III. EXPERIMENTAL CONSIDERATIONS

The experiment was performed at the alternating gradient synchrotron at Brookhaven National Laboratory using antiprotons in the low-energy separated beam of momentum 750 MeV/c.

The counter telescope is shown in Fig. 2. A coincidence of counters 1, 2, 3, and 4 indicated

BEAM

T,   UPSTREAM 4.5m

40 cm   8cm   60 cm

1 2   Č   DEGRADER 3 4   TARGET   5

12 cm   40 cm   Cu   Be

Pb

COAXIAL
DETECTOR

180 cm
TO FLOOR

$1 = 13 \times 13 \times 0.3 \text{ cm}^3$ $4 = 13 \times 13 \times 0.3 \text{ cm}^3$
$2 = 10 \times 10 \times 0.3 \text{ cm}^3$ $5 = 30 \times 30 \times 1.3 \text{ cm}^3$
$3 = 10 \times 10 \times 1.3 \text{ cm}^3$ $Č = 10 \times 10 \times 1.3 \text{ cm}^3$

FIG. 2. The beam telescope system of scintillation and Čerenkov counters to indicate an antiproton stop signature.

TABLE II. The targets and detectors that were used in the work reported here.

Target	Isotopic composition	Target thickness (g/cm^2)	Antiproton stops $(\times 10^6)$	Detector (cm^3)	Resolution (eV)
^6_3Li	6 (95%) 7 (5%)	4.1	168	1	441 at 26.9 keV
^7_3Li	6 (7.3%) 7 (92.7%)	5.8	86	1	450 at 27.5 keV
$^{nat}_6C$	12 (98.89%) 13 (1.11%)	7.6	82	1	466 at 40.5 keV
$^{nat}_{14}Si$	28 (92.21%) 29 (4.70%) 30 (3.09%)	16.3	53	15	965 at 107 keV
$^{31}_{15}P$	31 (100%)	9.8	29	15 50	1030 at 123 keV 947 at 123 keV
$^{nat}_{26}Fe$	54 (5.82%) 56 (91.66%) 57 (2.19%) 58 (0.33%)	9.1	29	50	1020 at 204 keV
$^{89}_{39}Y$	89 (100%)	12.6	27	50	1080 at 279 keV
$^{nat}_{40}Zr$ (ZrC)	90 (51.46%) 91 (11.23%) 92 (17.11%) 94 (17.40%) 96 (2.80%)	11.2	25	15 50	1180 at 294 keV 1100 at 294 keV
$^{133}_{55}Cs$ (CsF)	133 (100%)	6.6	11	50	1160 at 362 keV
$^{174}_{70}Yb$ (Yb$_2$O$_3$)	170 (0.04%) 171 (0.32%) 172 (0.91%) 173 (1.64%) 174 (96.58%) 176 (0.51%)	4	18	50	1250 at 403 keV

that a beam particle had entered the target. If the particle did not stop, it produced a signal in counter 5 which vetoed the event. The Lucite Čerenkov counter, which had an index of refraction of 1.4, vetoed pions. The 750 MeV/c pions produced light at 43°, while antiprotons produced no light. Antiprotons were distinguished from pions in the beam by a dE/dx requirement in counter 3 and time-of-flight information. Counter 4 was made as thin as possible without losing efficiency, because an antiproton stopping within counter 4 would register as a stop signature. It was used to define the time of the antiproton stop. Since pions from an antiproton annihilation in the target could trigger counter 5 and veto a good event, counter 5 was placed downstream from the target in order to minimize the solid angle for detection of pion emission, while still intercepting most of the beam. Counter T along with counter 4 provided time-of-flight information for the stop signature. Counter T was located just downstream of the mass slit, providing a 5 m path length. The timing resolution was 1.6 nsec, while the difference be-

tween pion and antiproton times of flgiht was 9 nsec.

Photons producing a signal in the lithium-drifted germanium [Ge(Li)] detector within 50 nsec of the stop signal were labeled prompt and stored in the "data" (or x-ray) spectrum. Those photon events whose time signatures occurred with delays up to 60 μsec after the stop were stored in the "calibration" spectrum.

Three Ge(Li) detectors were used in the collection of data: a 1 cm^3 planar, a 15 cm^3 semiplanar, and a 50 cm^3 coaxial. The small planar was used to detect x rays with energies below about 60 keV. The two larger detectors were sometimes used simultaneously for the higher-energy transitions. The detectors used and the resolution obtained for each target studied are listed in columns 5 and 6 of Table II. In columns 1–3 of Table II are listed the targets, their isotopic composition, and their thickness in the beam direction. Also listed in column 1 are the chemical forms of the compounds used. A listing of the sources used with energies and relative intensities of the lines along with the associated targets is given in Table III.

TABLE III. The sources that were used to calibrate and their energies. The relative intensities are given in parentheses.

Source	Energy (keV) (Intensity)				Targets
^{241}Am	11.890(0.070)	16.84(0.25)	20.12(0.011)	22.20(0.020)	C [a]
	13.760(0.121)	17.0607(0.14)	20.782(0.260)	26.345(0.193)	
	13.9441(0.97)	17.508(0.063)	21.11 $\left.\right\rbrace$ (0.047)	59.537(2.97)	
	15.876(0.029)	17.751(1.000)	21.340		
	16.13(0.019)	17.992(0.113)	21.488(0.077)		
^{57}Co	6.400	7.058	14.408		C, ^{6}Li, ^{7}Li [b]
^{137}Cs	31.817(54.3)	36.303(10.1)	37.270(7.0)		C, ^{6}Li, ^{7}Li, Yb [c]
	32.194(100)	36.378(19.5)	661.638		
^{133}Ba	53.155(3.54)	160.60(1.15)	302.851(29.9)		Zr, Cs, Yb [d]
	79.621(3.9)	223.11(0.75)	356.005(100)		
	80.997(52.6)	276.397(11.7)	383.851(14.2)		
^{75}Se	66.05(1.69)	121.115(28.0)	198.596(2.40)	279.528(42.2)	Zr, Cs [e]
	96.733(5.4)	136.000(95.6)	264.651(100)	303.916(2.2)	
^{182}Ta	65.7217(8.0)	113.6670(5.5)	179.3905(9.0)	264.071(10.4)	Si, P, Fe, Y [f]
	67.7495(118)	116.4149(1.27)	198.3477(4.4)		
	84.6805(7.6)	152.4281(20.5)	222.101(21.6)		
	100.1064(40.2)	156.3817(7.8)	229.316(10.4)		
^{203}Hg	279.191				Si, Yb
^{22}Na	511.0034				Yb

[a] R. L. Watson and T. K. Li, Nucl. Phys. A178, 201 (1971); J. L. Campbell and L. A. McNelles, Nucl. Instrum. Methods 117, 519 (1974).
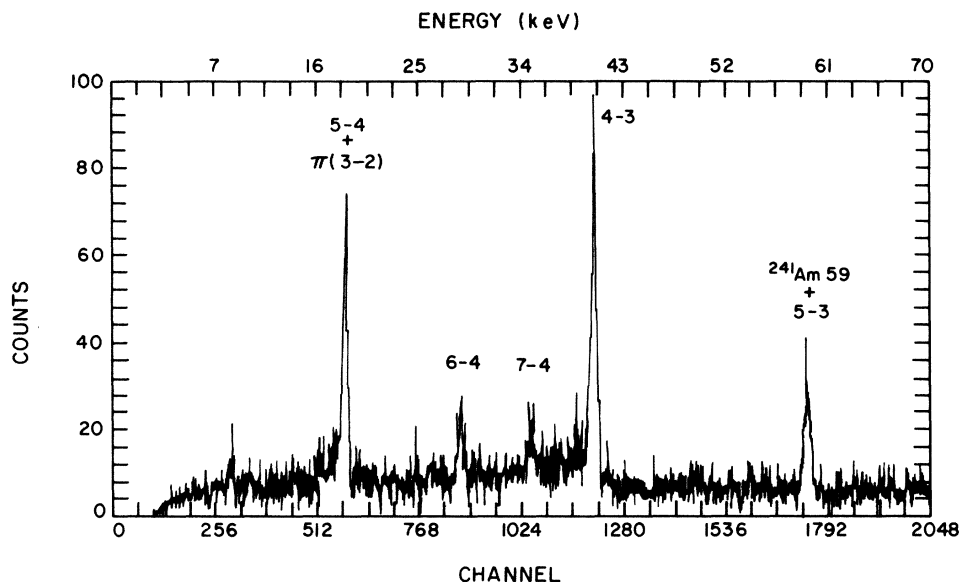[b] J. Rapaport, Nucl. Data B3, 4 (1970).
[c] R. L. Bunting, Nucl. Data Sheets 15, 335 (1975).
[d] E. A. Henry, Nucl. Data Sheets 11, 495 (1974).
[e] Reference 41.
[f] M. R. Schmorak, Nucl. Data Sheets 14, 559 (1975).

ENERGY (keV)

FIG. 3. An x-ray spectrum of $\bar{p}C$.

IV. DATA ANALYSIS

A. Form of the data

The spectra consisted of 2048 channels of calibration collected simultaneously with 2048 channels of data. Sample data spectra are presented in Figs. 3 through 5.

The data spectra included not only antiprotonic x-ray transitions but also other peaks associated with an antiproton stop. These peaks result from low-energy γ rays produced by nuclei de-exciting following $\bar{p}$ absorption, as well as from pionic and electronic x rays. The nuclear γ rays and the electronic x rays in the data spectra were used in consistency checks of the calibration method.

B. Peak shapes

The antiprotonic x-ray peaks all had some natural broadening, but only the broadening of the terminating radiative transition was large enough to be included in the fits. Naturally broadened trans-

ENERGY (keV)
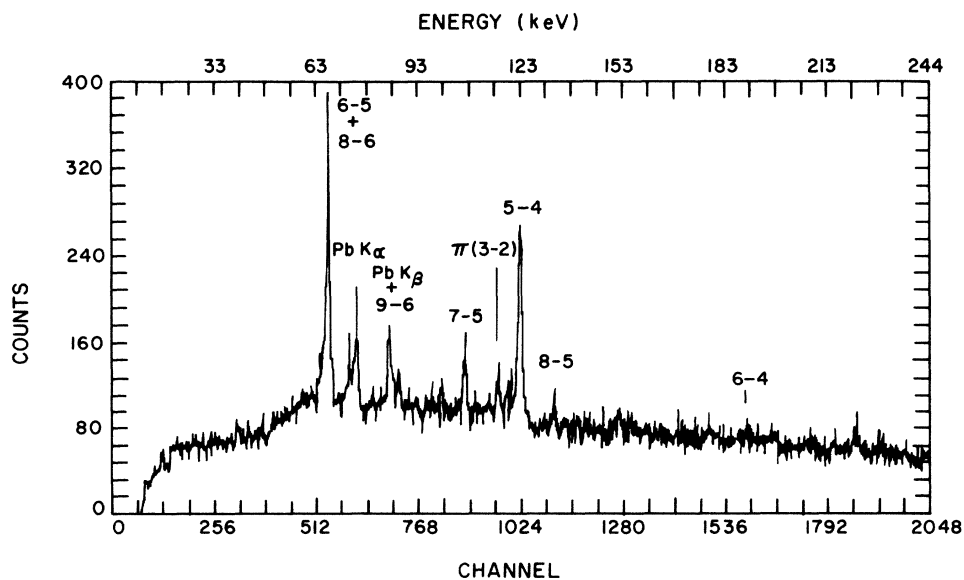
FIG. 4. An x-ray spectrum of $\bar{p}P$.
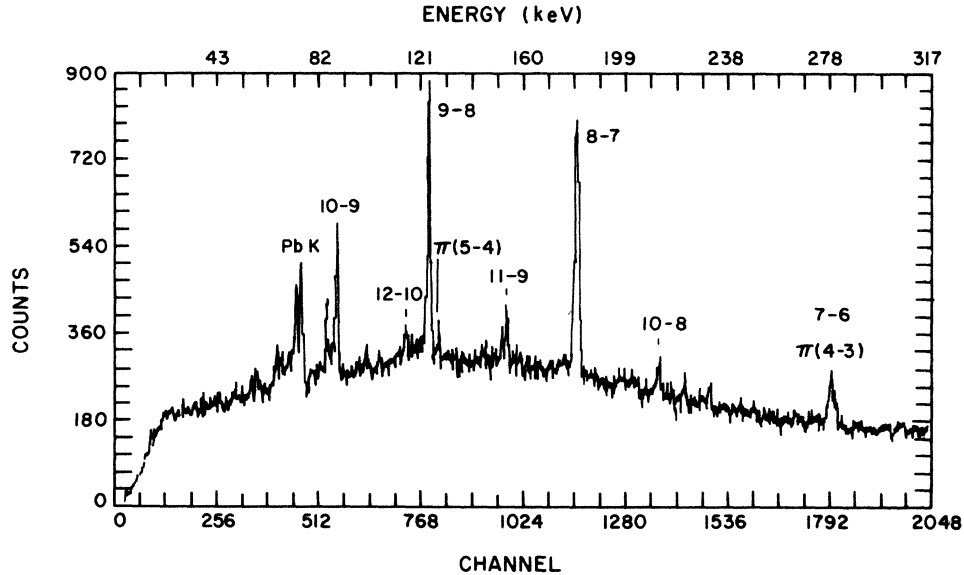
FIG. 5. An x-ray spectrum of $\bar{p}Y$.

itions obey a Lorentzian distribution in energy:

$$F_L(y) = H_L \frac{(\tfrac{1}{2}\Gamma)^2}{(y - y_0)^2 + (\tfrac{1}{2}\Gamma)^2} ,\qquad (13)$$

where H_L is the height, y_0 is the centroid, and Γ is the full width at half-maximum amplitude (FWHM).

In order to determine the peak shape given a natural broadening comparable to the detector resolution, a Gaussian function F_G representing the detector response was folded into the Lorentzian distribution. The result is known as a Voigtian distribution:

$$F_V(y) = \int_{-\infty}^{\infty} F_L(y - x) F_G(x) dx$$

$$= H_G H_L (\tfrac{1}{2}\Gamma)^2 \int_{-\infty}^{\infty} \frac{\exp[-(x)^2/2\sigma^2]}{(y - y_0 - x)^2 + (\tfrac{1}{2}\Gamma)^2} dx ,\qquad (14)$$

where σ is the standard deviation of the Gaussian and $H_G = 1/(\sqrt{2\pi}\,\sigma)$ in order to normalize the area of the Gaussian distribution to unity. This function was integrated numerically. The variables associated with the Gaussian function were determined from the calibration peaks and were held fixed in the Voigtian fits. We represented the background by a polynomial. Only the height, centroid, and width of the Lorentzian distribution and the backround parameters were varied to determine the best fit.

The peak shapes for most spectra contained low energy tails and, for a few spectra, high energy tails. This tailing was taken into account by modifying the Gaussian distribution, necessitating extra parameters. In the analysis several shapes were used: (1) Matching an exponential tail to a Gaussian distribution (one additional parameter),[13]

$$F_G(x) = \begin{cases} H_G \exp[-(x - x_0)^2/2\sigma^2], & x \ge x_0 - p_1^2 \\ H_G \exp[p_1^2(2x - 2x_0 + p_1^2)/2\sigma^2], & x \le x_0 - p_1^2; \end{cases}\qquad (15)$$

(2) adding an exponential function which goes to zero at the origin (two additional parameters),[14]

$$F_G = H_G \exp[-(x - x_0)^2/2\sigma^2] + \begin{cases} 0, & x \ge x_0 \\ H_G P_2 \left\{ 1 - \dfrac{1}{[(x - x_0)/\sqrt{2\sigma}]^2 + 1} \right\} \exp[p_1(x - x_0)/\sqrt{2\sigma}\,], & x \le x_0; \end{cases}\qquad (16)$$

(3) adding another Gaussian with a different width and centroid (three additional parameters),[15]

$$F_G(x) = H_G \exp[-(x - x_0)^2/2\sigma^2]$$

$$+ H_G P_2 \exp[-(x - x_0 - p_1)^2/2 p_3^2 \sigma^2].\qquad (17)$$

Shape (2) was used in most cases and could reproduce the peak shapes very well (see Fig. 6). When high-energy tailing was important, shape (3) gave the best fits.

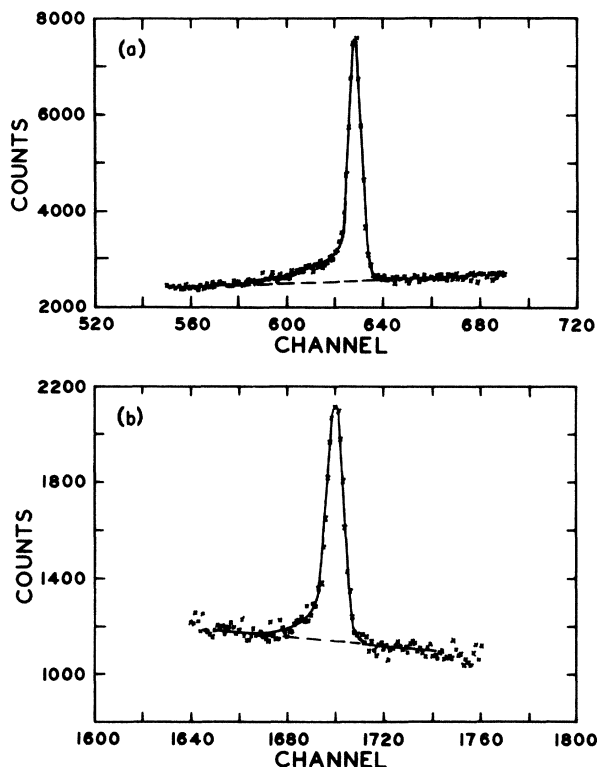An additional modification was required for high-

FIG. 6. The modified Gaussian distribution peak fits for the ^{182}Ta (a) 100 keV and (b) 264 keV source lines with Y calibration spectrum.

count peaks superimposed on a low background. The background used in these cases was a combination of a linear and a step function[16]:

$$B(x) = A + Cx + H_G h\, \mathrm{erf}[-(x - x_0)/\sigma_e],\qquad(18)$$

where erf(x) represents the error function. The variables to be determined were h and σ_e.

C. Method of analysis

The data for each target consisted of several independent (approximately 8 h) runs. The calibration of the summed runs was fitted with different peak shapes in order to determine the optimum shape. Very rarely, and only for transition peaks containing low statistics, were unmodified Gaussian distributions adequate. In most cases the dependence of additional parameters on energy had to be determined. This was done by fitting the calibration peaks, allowing all parameters to vary, and graphing the additional parameters as a function of energy.

The dependence of the peak width Δ_{FWHM} on the energy E is given by $\Delta_{(FWHM)}{}^2 = A^2 + B^2 E$, (19) where A represents the contribution due to the preamplifier noise and B is a function of the num-

ber of secondary electrons liberated in the detector.[17] A and B were determined from the calibration peak widths. The widths of unbroadened x-ray transition peaks were consistent with this parametrization. The width and additional parameters needed to specify the instrumental peak shape were held constant during the Voigtian distribution fits.

In fits of antiprotonic x-ray spectra, we assumed the theoretical fine-structure splitting. The Voigtian distribution fits to the terminating radiative transition determined the natural broadening, in addition to the transition energy. The strong interaction energy shift was defined as the measured energy minus the transition energy calculated solely from electromagnetic theory.

The x-ray intensity measurement of the last observable transition was used to determine the upper level width.

Theoretical estimates of intensities of antiprotonic x-ray transitions determined from cascade calculations which include strong interaction effects[18] were compared to the measured intensities. The strong interaction level widths and the initial populations of l sublevels for high-n levels were varied in order to reproduce measured intensities. A statistical population in the initial $n = 42$ level reproduced the measured intensities only for the lithium and carbon $\bar{p}$ atomic x rays. Agreement for the higher-Z target x-ray intensities required an initial distribution shifted toward the higher l sublevels.

The cascade analysis not only constituted a basic check of the detector efficiency and target absorption but also permitted the best estimate of the relative intensities of antiprotonic x-ray transitions coincidentally located at the same energy. For instance, a cascade calculation which reproduced the intensities of the measurable $\Delta n = 2$ and $\Delta n = 3$ transitions provided a good estimate of the intensity of the $n = 11$ to $n = 8$ transition, which was not resolved from the $n = 7$ to $n = 6$ transition in the Fe, Y, and Zr spectra. Also, the intensities of contributions of the transitions to noncircular levels were determined from these calculations.

D. Error analysis

The errors assigned to peak areas included a contribution due to the uncertainty in the separation of the background and peak. This conservative estimate of errors was made because Voigtian peaks decay slowly as distance from the centroid increases.

In addition to the statistical error, there were contributions to the errors on the Voigtian distribution due to the uncertainties in the width and additional parameters of the instrumental peak

shape and due to the variation of the best-fit parameters with the fitting interval. In general, the statistical error made the largest contribution to the total error. The contributions to the errors from the uncertainties in the modified Gaussian parameters were rarely significant, except in the case of phosphorous.

There were several background lines which had to be considered in the analysis. A pionic $n = 3$ to $n = 2$ x-ray transition was close in energy to the antiprotonic $n = 5$ to $n = 4$ x-ray transition for silicon and phosphorus. The pionic x-ray peak had to be included in the fitting, but did not significantly affect the errors on the $\bar{p}$ x-ray peaks. The analysis of the $\bar{p}$Fe $n = 6$ to $n = 5$ x-ray transition was complicated by the presence of the $\bar{p}$ $n = 8$ to $n = 6$ transition. In the fit we varied the amplitude of the $n = 8$ to $n = 6$ and all $n = 6$ to $n = 5$ parameters. A reasonable separation of these transitions could be made because the $n = 8$ to $n = 6$ peak was narrow, while that of the $n = 6$ to $n = 5$ transition was broadened.

The fits to the $\bar{p}$-yttrium and $\bar{p}$-zirconium data took into account the pionic $n = 4$ to $n = 3$ x-ray transition. The amount of contamination was determined from the pionic $n = 5$ to $n = 4$ x-ray transition whose energy is near that of the $\bar{p}$ $n = 9$ to $n = 8$ transition. Pionic x-ray measurements on yttrium and zirconium were either nonexistent or not sufficiently accurate. Calculations using the available semiphenomenological optical potential for pionic atoms were used to give the $n = 4$ to $n = 3$ pionic x-ray transition shift, width and yield to a sufficient accuracy. The largest contribution in the error due to the subtraction of the pionic $n = 4$ to $n = 3$ x-ray transition from the $\bar{p}$ data was due to the uncertainty in the intensity of the pionic $n = 5$ to $n = 4$ transition.

$n = 3$ to $n = 2$ *transition of* $\bar{p}$ ^6Li. The peak is 1.3 standard deviations above the background. There are no identifiable electronic x-ray or nuclear γ-ray patterns in the energy region of interest. The other peaks in the spectra indicate $\bar{p}$C x rays and $\bar{p}$O x rays. The $n = 6$ to $n = 4$ transition of $\bar{p}$C was resolved from the $n = 3$ to $n = 2$ $\bar{p}$^{6}Li transition and included in the fit.

$n = 3$ to $n = 2$ *transition of* $\bar{p}$ ^7Li. The peak is 2.6 standard deviations above the background. There are no identifiable electronic x-ray patterns or nuclear γ rays in the energy region of interest. $\bar{p}$C x rays are present, but with much less intensity than in the ^{6}Li spectrum. The intensity of the $\bar{p}$C $n = 6$ to $n = 4$ transition was determined using the $\bar{p}$C $n = 6$ to $n = 5$ and $n = 5$ to $n = 4$ transitions.

$n = 8$ to $n = 7$ *transition of* $\bar{p}$Cs. The background is consistent with no peak. We can give only an upper limit of 0.25 on the relative yield at the 90%

confidence level.

$n = 9$ to $n = 8$ *transition of* $\bar{p}$ ^{174}Yb. The peak was 4.1 standard deviations above the background, and was consistent with a large fine structure and large Lorentzian width. The pionic $n = 5$ to $n = 4$ transition was resolved from the $\bar{p}$ ^{174}Yb $n = 9$ to $n = 8$ transition and was included in the fit. The intensity of the pionic x-ray line was determined independently. A nuclear γ ray from the second excited state of ^{162}Tb could contaminate the $n = 9$ to $n = 8$ $\bar{p}$Yb transition line. The decay to the first excited state or ground state results in two γ rays of approximately equal intensity with energies 402.8 ± 0.3 keV and 441.6 ± 0.3 keV.[19] The intensities of the γ rays should be small compared to the total number of $\bar{p}$ x rays because of the small probability that capture of the $\bar{p}$ in Yb can result in ^{162}Tb production. An upper limit of 13% of the intensity of the $\bar{p}$Yb $n = 9$ to $n = 8$ transition intensity was put on the 402.8 keV nuclear γ-ray line by noting the absence of the 441.6 keV line in the data spectrum. The error on the $\bar{p}$Yb $n = 9$ to $n = 8$ x-ray intensity is over twice this amount. Because there is no definite evidence that these nuclear γ rays are present in the data spectrum, the 402.8 keV line was not included in the Voigtian fit.

V. RESULTS

A. Results of the fits to the x-ray peaks

The measured antiprotonic atom x-ray energies are presented in Table IV along with the calculated electromagnetic energies. The calculated energies are the weighted average of those of the fine-structure components, assuming a statistical population of the multiplet members. The energies measured for $\bar{p}$ ^{6}Li, $\bar{p}$ ^{7}Li, and $\bar{p}$ ^{174}Yb x-ray transitions have been corrected for the presence of the contaminant isotopes listed in Table II. Both the measured and the calculated energies for the other elements represent an average over the isotopic composition. The measured energies have also been corrected for the presence of transitions to noncircular levels, based on the cascade calculation which most nearly reproduced the x-ray intensities. The correction was never greater than the error on the energy.

Several Voigtian distribution peak fits are presented in Figs. 7 and 8. The strong interaction parameters resulting from these fits are given in Table V. The shifts are the measured energies minus the calculated electromagnetic energies of Table IV.

The wave function of the $\bar{p}$ in the $n = 6$ state of the $\bar{p}$Zr atom should have a larger overlap with the nucleus than that of the $\bar{p}$Y $n = 6$ level and thus the strong interaction width and shift of the $\bar{p}$Zr level

TABLE IV. Measured and calculated $\bar{p}$ x-ray transition energies for the important transitions. The measurements marked with an asterisk were not used in the determination of the mass of the antiproton. The calculated energies are the weighted averages of those of the fine structure components.

| Element and transition	Measured energy (keV)	Electromagnetic energy (keV)
^{6}Li 4-3	9.401 ± 0.011	9.388
5-3	13.703 ± 0.043	13.730
6-3	16.114 ± 0.078	16.112
3-2*	26.81 ± 0.17	26.882
^{7}Li 4-3	9.575 ± 0.008	9.586
5-3	13.970 ± 0.030	14.018
6-3	16.487 ± 0.042	16.447
3-2*	27.177 ± 0.081	27.445
^{nat}C 5-4	18.745 ± 0.012	18.734
6-4	28.893 ± 0.018	28.894
7-4	35.072 ± 0.034	35.020
4-3*	40.539 ± 0.010	40.543
^{nat}Si 6-5	58.08 ± 0.11	58.061
5-4*	107.005 ± 0.039	107.043
^{nat}P 6-5	66.953 ± 0.060	66.886
7-5	107.091 ± 0.049	107.140
8-5	133.20 ± 0.10	133.254
5-4*	123.249 ± 0.023	123.314
6-4*	189.85 ± 0.32	190.149
^{nat}Fe 10-8	93.74 ± 0.10	93.644
8-7	79.827 ± 0.064	79.752
9-7	134.19 ± 0.17	134.333
7-6	123.21 ± 0.18	123.010
8-6	202.78 ± 0.17	202.686
6-5*	204.28 ± 0.31	204.292
^{nat}Y 12-10	115.21 ± 0.14	115.213
10-9	88.584 ± 0.024	88.572
11-9	154.022 ± 0.046	153.991
9-8	123.927 ± 0.016	123.933
10-8	212.36 ± 0.15	212.408
8-7	180.942 ± 0.019	180.957
7-6*	279.03 ± 0.16	279.183
^{nat}Zr 12-10	121.43 ± 0.15	121.242
10-9	93.181 ± 0.054	93.209
11-9	162.075 ± 0.064	162.050
9-8	130.412 ± 0.018	130.423
10-8	223.461 ± 0.073	223.527
8-7	190.422 ± 0.019	190.441
7-6*	293.36 ± 0.10	293.811
^{nat}Cs 10-9	177.12 ± 0.19	177.095
9-8	247.86 ± 0.19	247.844
8-7*	...	361.987
^{174}Yb 11-10*	212.607 ± 0.074	212.748
10-9*	287.953 ± 0.088	287.934 ± 0.020
9-8*	403.76 ± 0.45	403.495 ± 0.090
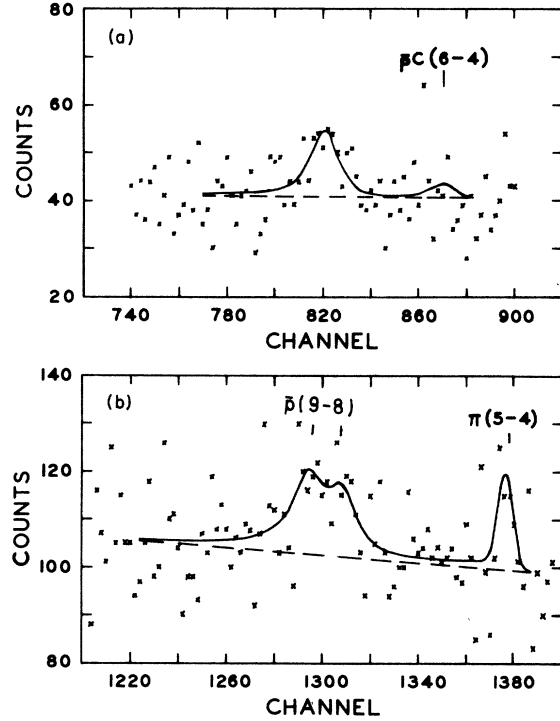
FIG. 7. The Voigtian distribution peak fits for the (a) $n = 3$ to $n = 2$ $\bar{p}$ x-ray transition of ^{7}Li and the (b) $n = 9$ to $n = 8$ $\bar{p}$ x-ray transition of ^{174}Yb.
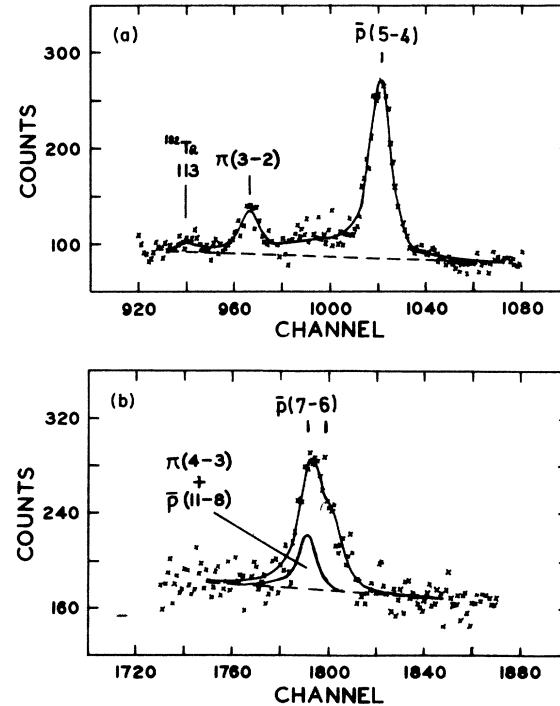

FIG. 8. The Voigtian distribution peak fits for the (a) $n = 5$ to $n = 4$ $\bar{p}$ x-ray transition of P and (b) the $n = 7$ to $n = 6$ $\bar{p}$ x-ray transition of Y.

TABLE V. Strong interaction measurements from the $\bar{p}$ x-ray transitions.

Element	Level	Shift (eV)	Width (eV)	Relative yield
^{6}Li	$2p$	-70 ± 170	340 ± 310	0.026 ± 0.021
	$3d$		$0.34(^{+1.45}_{-0.16})$	
^{7}Li	$2p$	-268 ± 81	180 ± 140	0.031 ± 0.012
	$3d$		$0.27(^{+0.18}_{-0.08})$	
C	$3d$	-4 ± 10	42 ± 18	0.516 ± 0.088
	$4f$		$0.036(^{+0.015}_{-0.011})$	
Si	$4f$	-38 ± 39	110 ± 190	$\cdots$
P	$4f$	-65 ± 23	446 ± 69	0.236 ± 0.024
	$5g$		$1.69(^{+0.25}_{-0.20})$	
Fe	$5g$	-10 ± 310	540 ± 320	0.32 ± 0.13
	$6h$		$4.0(^{+3.9}_{-1.7})$	
Y	$6h$	-150 ± 160	800 ± 320	0.375 ± 0.057
	$7i$		$6.8(^{+4.9}_{-4.4})$	
Zr	$6h$	-450 ± 100	700 ± 210	0.418 ± 0.057
	$7i$		$6.4(^{+4.7}_{-3.3})$	
Cs	$7i$	$\cdots$	$\cdots$	<0.25
	$8j$		>25	
Yb	$8j$	260 ± 460	1480 ± 660	0.295 ± 0.093
	$9k$		$27(^{+18}_{-9})$	

should be larger. However, the observed width indicates less overlap whereas the shift indicates more overlap. Roberts et al.[20] have reported similar results for kaonic atoms. They found a smaller strong-interaction width of the K^- Sn ($Z = 50$) level than the width of the corresponding K^- In ($Z = 49$) level.

B. Optical-model analysis

In principle it is possible to use neutron and proton densities directly instead of an average matter density in an optical potential. However, the limited precision of the available data dictated the use of an effective scattering length based on the assumption that the neutron and proton densities are essentially identical.

We interpreted the measured shifts and widths in terms of a phenomenological potential of the form mentioned in Sec. IIC [Eq. (12)].

In the analysis we assumed that the matter densities could be represented by the *charge* densities which have been determined from muonic atom[21] and electron scattering data.[22] A Fermi distribution was assumed,

$$\rho(r) = \rho_0\{1 + \exp[4\ln3(r - c)/t]\}^{-1}, \qquad (20)$$

where c and t are the half-density radius and skin-thickness parameters, respectively. A better description of low-Z nuclei can sometimes be obtained using a harmonic oscillator distribution

$$\rho(r) = \rho_0[1 + \alpha(r/c)^2]\exp[-(r/c)^2], \qquad (21)$$

where α and c are parameters. Unfortunately, the muonic atom and electron scattering results are not sensitive to the nuclear periphery. Because the $\bar{p}$-nucleon absorption takes place on the periphery, the tabulated values of c and t may not provide the best density estimate for this region. Also, we note that the upper level widths are more dependent on the density distribution which is selected than the lower level shifts and widths because nuclear absorption takes place farther from the half-density radius for the upper atomic levels.

It is interesting to note that at the present level of experimental precision, it is not critical whether one uses a complex Dirac equation or a complex Klein-Gordon equation in order to calculate the antiprotonic atom energy eigenvalues. When we compared the Dirac solutions (averaged over the fine-structure components) to those of the Klein-Gordon equation, the differences were typically 4% for the stong interaction shift and 1% for the width. Since the smallest errors on the shifts and widths were 22% and 15%, respectively, we decided to carry out the general analysis with the Klein-Gordon equation.

The additional vacuum polarization energy corrections to the Dirac energies[23] due to the strong interaction were calculated to be 0 eV for the $n = 3$ level of $\bar{p}$C, -1 eV for the $n = 4$ level of $\bar{p}$Si, -2 eV for the $n = 4$ level of $\bar{p}$P, -4 eV for the $n = 5$ level of $\bar{p}$Fe, -6 eV for the $n = 6$ level of $\bar{p}$Y, -8 eV for the $n = 6$ of $\bar{p}$Zr, and -14 eV for the $n = 8$ level of $\bar{p}$Yb. These corrections were small com-
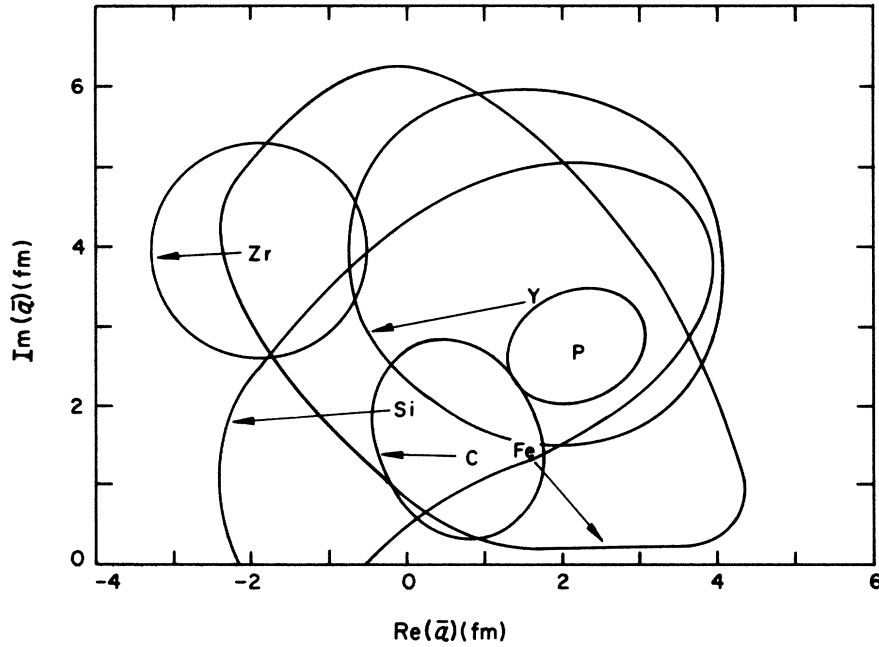
FIG. 9. The several independent determinations of the effective scattering length $\bar{a}$ from the lower-level shifts and widths.

pared to the experimental errors and were considered part of the total strong interaction.

The measurements of the $\bar{p}$ x-ray transitions in ^{6}Li, ^{7}Li, and ^{174}Yb were not used in the determination of the effective scattering length. These measurments, with their large errors, have

little effect on the final determination of the effective scattering length.

The relationship between the effective scattering length and measured numbers was determined using a computer program by Koch and Sternheim.[24] A χ^2 function defined by
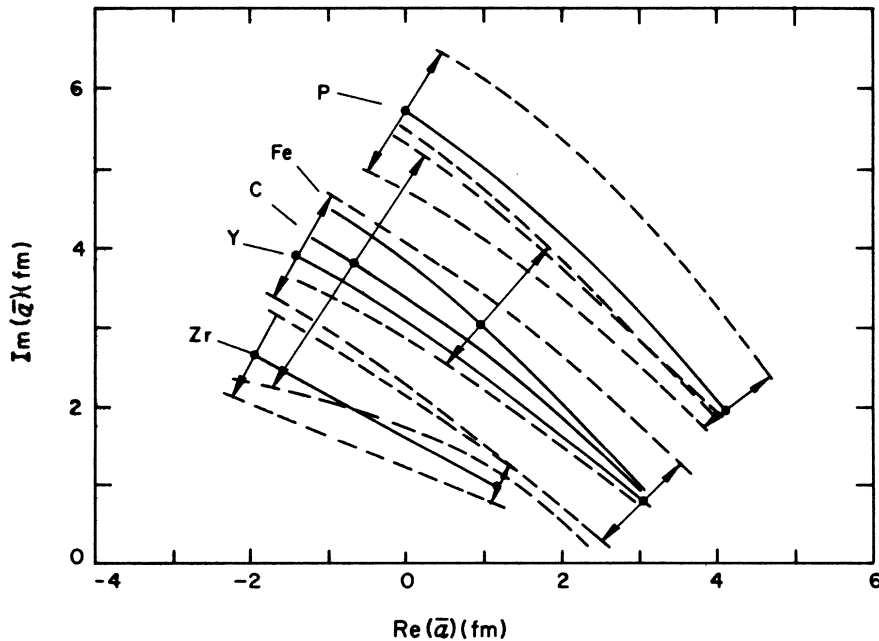
FIG. 10. The restrictions placed on the effective scattering length $\bar{a}$ from the upper-level widths.

TABLE VI. Measured and calculated strong interaction shifts and widths for the n values shown. The measurements marked with an asterisk were used to determine the optical potential effective scattering length $\bar{a}$. The calculated values were obtained using the best-fit value of $\bar{a}$. Results from previous work are also included.

| Nucleus | n (level) | Measured (eV) | | | Calculated (eV)[a] | | | Nuclear distribution parameters |
		E_n	Γ_n	Γ_{n+1}	E_n	Γ_n	Γ_{n+1}	
${}^{6}_{3}$Li	2	-70 ± 170	340 ± 310	$0.34\,(^{+1.45}_{-0.18})$	-228	408	0.164	HO 1.72, 0.330[b]
					-321	678	0.231	2pF 1.87, 2.3[c]
					-222	308	0.023	2pF 1.70, 1.0
${}^{7}_{3}$Li	2	-268 ± 81	180 ± 140	$0.27\,(^{+0.18}_{-0.08})$	-265	444	0.205	HO 1.72, 0.327[b]
					-361	731	0.270	2pF 1.75, 2.3[c]
					-227	313	0.024	2pF 1.60, 1.0
${}^{12}_{6}$C	3	-4 ± 10	$42 \pm 18^{*}$	$0.036\,(^{+0.015}_{-0.011})^{*}$	-11	54	0.034	2pF 2.04, 2.3[d]
					-12	37	0.018	HO 1.69, 1.067[b]
${}^{nat}_{14}$Si	4	-38 ± 39	$110 \pm 190^{*}$	$\cdots$	-36	177	0.441	2pF 3.14, 2.3[d]
					-38	193	0.495	2pF 3.14, 2.36[e]
${}^{31}_{15}$P	4	$-65 \pm 23^{*}$	$446 \pm 69^{*}$	$1.69\,(^{+0.25}_{-0.20})^{*}$	-83	353	1.12	2pF 3.30, 2.3[d]
					-89	409	1.38	2pF 3.21, 2.46[e]
${}^{nat}_{26}$Fe	5	-10 ± 310	$540 \pm 320^{*}$	$4.0\,(^{+3.9}_{-1.7})$	-122	554	3.7	2pF 4.12, 2.3[d]
					-104	500	3.2	2pF 3.97, 2.6[e]
${}^{89}_{39}$Y	6	$-150 \pm 160^{*}$	$800 \pm 320^{*}$	$6.8\,(^{+1.9}_{-1.4})^{*}$	-137	661	7.1	2pF 4.87, 2.3[d]
					-147	734	8.1	2pF 4.86, 2.38[e]
${}^{nat}_{40}$Zr	6	$-450 \pm 100^{*}$	$700 \pm 210^{*}$	$6.4\,(^{+1.7}_{-1.3})^{*}$	-194	880	10.2	2pF 4.91, 2.3[d]
${}^{133}_{55}$Cs	7	$\cdots$	$\cdots$	>25	-239	1061	18.1	2pF 5.67, 2.3[d]
${}^{174}_{70}$Yb	8	260 ± 460	1480 ± 660	$27\,(^{+18}_{-9})$	-105	536	9.9	2pF 6.23, 2.18[f]
					-300	1216	28.6	2pF 7.00, 2.3
${}^{4}_{2}$He	2	$\cdots$	191 ± 170^{g}	$\cdots$	-36	111	0.0048	2pF 1.00, 2.3
					-49	132	0.0067	2pF 1.70, 2.3
${}^{14}_{7}$N	3	-39 ± 51^{h}	173 ± 34^{h}	$\cdots$	-42	170	0.167	2pF 2.14, 2.3[d]
					-36	116	0.095	2pF 2.43, 1.87[i]
					-48	122		HO 1.76, 1.291[b]

$$\chi^2 = \left(\frac{E_{meas}-E_{calc}}{\Delta E}\right)^{2} + \left(\frac{\Gamma_{meas}-\Gamma_{calc}}{\Delta\Gamma}\right)^{2}, \qquad (22)$$

was calculated, where $\Gamma_{meas} \pm \Delta\Gamma$ is the observed width, $E_{meas} \pm \Delta E$ the observed transition energy, and "calc" refers to the corresponding values calculated assuming various values of $\bar{a}$.

Figure 9 is a graph of the complex $\bar{a}$ plane for the shifts and widths of the lower states. The position of the $\chi^2_{min} + 1$ contours about the central points are used to represent one standard deviation. The upper-level width for each target can be used to obtain a line running across the complex $\bar{a}$ plane. Figure 10 contains this information. The data for phosphorus and zirconium are least in agreement with all other targets for both upper and lower levels. This disagreement indicates a systematic error, such as inaccurate matter distributions, real differences in nuclear structure beyond that accounted for by differing matter distributions,

or an inadequate optical model potential.

Columns 3, 4, and 5 of Table VI contain a summary of measured antiprotonic atom shifts and widths. Column 9 contains the values of c and t used to calculate the shifts and widths shown in columns 6, 7, and 8. The measurements marked with an asterisk were used to determine the best-fit value of $\bar{a}$:

$$\bar{a} = [(0.85 \pm 0.38) + i(2.66 \pm 0.28)]\ \text{fm}. \qquad (23)$$

A value of $\bar{a}$ was also determined using only the measurements reported here as well as these measurements excluding the shift in $\bar{p}$Zr. The results are reported in Table VII. It should be noted that a previously quoted value[25] for $\bar{a}$, namely,

$$\bar{a} = [2.9\,(^{+1.4}_{-1.0}) + i1.5\,(^{+1.2}_{-0.6})]\ \text{fm}, \qquad (24)$$

was obtained using the values $c, t = 2.43, 1.87$ fm for ^{14}N and 2.60, 2.20 fm for ^{16}O. Using the more recently tabulated values[21] from muonic-atom

TABLE VI. (Continued)

Nucleus	n (level)	Measured (eV)			Calculated (eV)[a]			Nuclear distribution parameters
		E_n	Γ_n	Γ_{n+1}	E_n	Γ_n	Γ_{n+1}	
${}^{16}_{8}O$	3	-60 ± 73[h]	648 ± 150[h]	...	-147	481	0.744	$2pF$ 2.44, 2.3[d]
					-151	461	0.703	$2pF$ 2.60, 2.20[i]
					-147	324		HO 1.805, 1.544[b]
${}^{16}_{8}O$	3	-120 ± 40[j*]	...	0.67 ± 0.15[j]	-147	481	0.744	$2pF$ 2.44, 2.3[d]
${}^{18}_{8}O$	3	-180 ± 50[j*]	...	0.90 ± 0.18[j]	-178	542	0.908	$2pF$ 2.54, 2.3[d]
${}_{15}P$	4	...	...	$1.14(^{+0.25}_{-0.19})$[k]	-83	353	1.12	$2pF$ 3.30, 2.3[d]
${}_{16}S$	4	-80 ± 40[k]	310 ± 180[k]	$3.04(^{+0.70}_{-0.51})$[k]	-152	595	2.26	$2pF$ 3.35, 2.3[d]
		-41 ± 44[j]	760 ± 110[j]	$2.85(^{+0.63}_{-0.46})$[j]				
${}_{17}Cl$	4	...	...	$8.00(^{+2.22}_{-1.48})$[k]	-137	1074	5.18	$2pF$ 3.53, 2.3[d]
${}_{19}K$	4	...	...	$26.8(^{+7.0}_{-4.7})$[k]	-908	2607	18.2	$2pF$ 3.66, 2.3[d]
${}_{50}Sn$	7	...	...	$3.07(^{+1.8}_{-1.3})$[k]	-43	272	3.25	$2pF$ 5.46, 2.3[d]
${}_{53}I$	7	...	...	$9.93(^{+7.7}_{-4.1})$[k]	-115	596	8.67	$2pF$ 5.60, 2.3[d]
${}_{59}Pr$	7	...	...	$24.7(^{+56}_{-14})$[k]	-565	2207	46.4	$2pF$ 5.80, 2.3[d]

[a] $\bar{a} = (0.85 + i2.66)$ fm.

[b] Harmonic oscillator distribution specified by (c, α) from Ref. 22.

[c] Two-parameter Fermi distribution with c chosen to agree with the HO distribution (Ref. 22) at the half density point.

[d] (c, t) from muonic atoms (Ref. 21) used in the $\bar{a}$ determination if the target data is marked with an asterisk.

[e] (c, t) from electron scattering (Ref. 22).

[f] This (c, t), together with $\beta = 0.323$, describe the deformed nucleus with a three parameter Fermi distribution (Ref. 21).

[g] M. Eckhause et al., Phys. Rev. C 11, 1056 (1975).

[h] Reference 25.

[i] Used in the previous $\bar{a}$ determination (Ref. 25).

[j] L. Tauscher, in High Energy Physics and Nuclear Structure, edited by D. E. Nagle et al., (AIP, New York, 1975).

[k] H. Koch, in Proceedings of the Fifth International Conference on High Energy Physics and Nuclear Structure, edited by G. Tiball (North-Holland, Amsterdam, 1975).

studies, of $c, t = 2.14, 2.3$ fm (^{14}N) and $2.44, 2.3$ fm (^{16}O), we obtain the value $\bar{a} = 1.2 + i2.5$ fm, in better agreement with the present result given in Eq. (23).

The sensitivity of the calculated values for the shift and width on either c or t separately is nearly linear. Table VIII gives the variations for the $n = 4$ $\bar{p}$ P level. A 10% variation of c or t causes the shift and width to change by about one standard deviation from the measured values. Because the experimental error on the value of c is 1% for P, the matter distribution parameters are known very well and the greatest uncertainty is the extrapolation of the distribution to the nuclear periphery.

The half-density radii determined from muonic-atom studies for ^{6}Li and ^{7}Li have large errors.[21] The values of c used were those which matched

TABLE VII. Comparison of the determinations of the phenomenological effective scattering length.

Data used for the fit	Best fit value of $\bar{a}$ (fm)	χ^2/degrees of freedom
All measurements marked with an asterisk in Table VI	$(0.85 \pm 0.38) + i(2.66 \pm 0.28)$	25.1 / 14
Present measurements	$(0.63 \pm 0.42) + i(2.73 \pm 0.32)$	23.1 / 10
Present measurements excluding the shift in zirconium	$(0.89 \pm 0.42) + i(2.49 \pm 0.34)$	16.7 / 9

TABLE VIII. Variations of the calculated shifts and widths with the nuclear shape parameters c and t for phosphorus. The phenomenologically determined effective scattering length was used in the calculations. ($\bar{a}$ = $(0.85 + i2.66)$ fm. $c, t = 3.304 \pm 0.029$, 2.3 fm (Ref. 21). Phosphorus measurements E_n, $\Gamma = -65 \pm 23$, 446 ± 69 (eV).

	$t = 2.3$ fm			$c = 3.304$ fm	
c (fm)	E_n	Γ (eV)	t (fm)	E_n	Γ (eV)
3.00	−62	295	2.02	−64	246
3.30	−83	353	2.30	−83	353
3.60	−110	421	2.55	−105	479

the harmonic oscillator distributions (from electron scattering[22]) at the half-density radii. Using harmonic oscillator distributions, or Fermi distributions with these values for c, we find that the only serious disagreement with measurement is with the width of the $n = 2$ level for $\bar{p}\,^7$Li. Smaller values for c and t result in improved agreement for the lower-level shifts and widths at the expense of poorer agreement for the upper-level width. A matter distribution which falls off more slowly than either the harmonic oscillator or the Fermi distribution is indicated.

If the values for c and t for Yb are increased, we can accurately reproduce the experimentally determined widths. Although a positive shift cannot be obtained using the strong interaction potential determined from the other x-ray measurements, the large error in the energy shift for the $n = 8$ level of $\bar{p}$ Yb makes this an insignificant problem.

Alberg, Henley, and Wilets[26] have developed a microscopic strong-interaction potential for kaonic atoms which was found to be very dependent on the binding energies of the outer nucleons. It was found that decreasing the binding energy resulted in an increase in the shift and a decrease in the width of the kaonic atom levels. This effect is confirmed in $\bar{p}$ Zr, but not in $\bar{p}$ Y. However, a comparison of the outer nucleon binding energies for ^{89}Y and the isotopes of Zr did not reveal any striking differences.

The effective scattering length given by Eq. (23) does not agree with the free scattering length given by Bryan and Phillips,[27] namely, $-0.88 + i0.81$ fm. This discrepancy indicates that effects due to the presence of bound nucleons or the below-threshold nature of the scattering are not properly taken into account. In addition, the existence of antiproton-nucleon resonances near threshold[28] could modify the effective scattering length.

Due to the uncertainties in the extrapolation of

the nuclear matter distribution to the nuclear tail and the nature of the antiproton-nucleus interaction, no additional information can be obtained by including short-range interactions, as suggested by Deloff and Law.[29] In addition, the relative importance of the kaon-two nucleon annihilations has been measured to be about 20% for emulsion nuclei,[30] an amount which indicates that it is a fairly important process. However, the presence of the K^--proton resonance below threshold plays an important role in the theoretical explanation of this effect,[31] while the corresponding resonance of the antiproton-nucleon system near threshold[28,32] is expected to have a much smaller effect. Therefore, the proportion of $\bar{p}$-two nucleon annihilations is probably much less than 20%. No definite conclusions can be reached because of the possibility of below-threshold resonances and the inaccuracy of the calculational techniques.[31] A parameter which would describe correlations at the nuclear surface[33] would be totally undetermined. The quality of the data and the theoretical understanding of the annihilation process are not sufficient to warrant inclusion of such a parameter.

The energy level of one member of the fine-structure doublet is affected more by the strong interaction than the other. The lower state, corresponding to the higher-energy transition, is shifted more, decreasing the fine structure. Because the relative intensity of the transitions is determined from the population of the upper levels, one would expect only a small deviation from intensities calculated with statistical populations.

An easily tested quantity was the fine-structure splitting. It was varied for the $n = 7$ to $n = 6$ transition of $\bar{p}$ Y, keeping the widths and relative populations constant. The experimentally determined fine structure was 1.17 ± 0.27 keV, to be compared with the theoretical value of 1.18 keV. This result does not put any restrictions on the strong-interaction potential parameters of Nishimura and Fujita,[34] which allows for relative changes in the shifts and widths beyond what would be expected due to different energies and wave functions of the fine structure levels.

We cannot reliably extract a "neutron halo" parameter as suggested in other work reported earlier[35] because of apparent uncertainties in the interpretation of the number of charged pions resulting from $\bar{p}$ absorption.[36]

C. Mass of the antiproton and other measurements

In the calculation of the transition energies presented in Table IV it was assumed that the mass of the antiproton and proton were identical. However, it is also possible to adjust the mass of the

TABLE IX. The determination of the antiproton mass from the measured x-ray energies. Other measurements are listed for comparison. Previous measurements: 938.3 ± 0.5 MeV, Ref. 38; 938.30 ± 0.13 MeV, Ref. 39; 938.179 ± 0.058 MeV, Ref. 40.

Element	$\frac{\Delta m_{\bar{p}}}{m_{\bar{p}}}(\times 10^4)$
^{6}Li	11 ± 13
^{7}Li	-13.0 ± 8.5
C	5.2 ± 4.3
Si	3 ± 20
P	-2.8 ± 3.6
Fe	6.3 ± 4.6
Y	-0.38 ± 0.76
Zr	-0.94 ± 0.77
Cs	0.9 ± 6.2
Average	-0.54 ± 0.52
$\bar{p}$ mass	938.229 ± 0.049 MeV
p mass	938.2796 ± 0.0027 MeV [a]

[a]Review of particle properties, Phys. Lett. **50B**, 1 (1974).

antiproton to give the best fit to the measured transition energies. Because the transition energies E are directly proportional to the reduced mass μ of the $\bar{p}$-nucleus system, the required adjustment would be

$$\frac{\Delta m_{\bar{p}}}{m_{\bar{p}}} = \frac{m_{\bar{p}}}{\mu}\frac{\Delta\mu}{\mu} = \frac{m_{\bar{p}}}{\mu}\frac{\Delta E}{E} . \tag{25}$$

Only those transitions unshifted by the strong interaction were used.[37] Table IX gives the ratio $\Delta m_{\bar{p}}/m_{\bar{p}}$ for each of the targets. The resulting $\bar{p}$ mass is within 1 standard deviation of the proton mass. Also presented in Table IX are three earlier[38-40] determinations of the $\bar{p}$ mass based on $\bar{p}$-atom measurements.

The present measurement for the $\bar{p}$ mass depends primarily on the $\bar{p}$Y and $\bar{p}$Zr data. The uncertainty in the x-ray energies of the ^{75}Se source made a substantial contribution to the errors in the Zr x-ray transition energies. The energies of the two important ^{75}Se source lines used for the determination of the $\bar{p}$ mass from the Zr data are[41] 136.000 ± 0.005 keV and 264.651 ± 0.008 keV. A change of these energies by more than one standard deviation would have a substantial effect. On the other hand, a correspondingly large shift in the energies of ^{182}Ta lines would not change the $\bar{p}$ mass measurement obtained from the Y data.

In the calculation of the electromagnetic energies, we assumed that the antiproton had a point-like structure. However, the antiproton is polarized by the large electric field produced by the nucleus at distances characteristic of radii of the lower-lying antiprotonic atom levels. Ericson

TABLE X. Nuclear γ rays that were observed in association with a $\bar{p}$ stop signature for the various targets listed.

Target	Measured energy (keV)	Tentative identification [a] (excited states of)
^{nat}Fe	125.883 ± 0.052	^{55}Mn (125.9 ± 0.1)
	156.193 ± 0.061	^{54}Mn (156.9 ± 1.0)
	159.340 ± 0.055	^{47}Ti (158.8 ± 0.5)
	211.71 ± 0.13	^{54}Mn (212 ± 1)
	226.317 ± 0.077	^{50}V (226.2 ± 0.1)
^{89}Y	231.93 ± 0.12	^{85}Sr (231.69 ± 0.10)
^{nat}Zr	231.61 ± 0.17	^{85}Sr (231.69 ± 0.10)

[a]The energies are taken from the Nuclear Data tables.

and Hüfner[42] have made an order-of-magnitude estimate of the energy shift $\Delta E_{\bar{p}\,pol}$ due to antiproton polarization,

$$\Delta E_{\bar{p}\,pol}(nlj) \simeq \frac{1}{3}\frac{Z^2}{A^{5/3}} \Delta E_{NP}(nlj) , \tag{26}$$

where ΔE_{NP} is the *nuclear* polarization contribution to the electromagnetic energy. This estimate increases the $n=7$ to $n=6$ $\bar{p}$Zr and $\bar{p}$Y transition energies by 2 eV and the $n=8$ to $n=7$ transitions by less than 1 eV. If the $n=8$ to $n=7$ transition energies were used to determine the antiproton polarizability (with $n=9$ to $n=8$ transitions as reference points), the result would have the opposite sign of the Ericson and Hüfner[42] estimate, but would include their value within the error.

The spectra accumulated during data runs contained several $\bar{p}$ stop-associated photon peaks which could not be identified as $\bar{p}$ atomic x rays, pionic atom x rays, electronic x rays, or source lines which were electronically misrouted. These peaks were identified as prompt nuclear γ rays. In Table X are listed the targets, the energies measured, and the tentative identification of these x-ray lines. Wiegand and Godfrey[43] also have observed the nuclear γ rays from ^{55}Mn and ^{47}Ti in K^- ^{56}Fe spectra.

Finally, we wish to report that during the accumulation of the $\bar{p}$P data, we obtained enough statistics to determine the energy and the strong interaction width of the pionic phosphorus $n=3$ to $n=2$ transition:

$$E_\pi(3-2) = 116.79 \pm 0.08 \text{ keV} ,$$

$$\Gamma_\pi(2p) = 0.31 \pm 0.11 \text{ keV} .$$

These values are consistent with those reported previously by Backenstoss.[44]

[1] H. A. Bethe and E. E. Salpeter, *Quantum Mechanics of One and Two Electron Atoms* (Springer-Verlag, Berlin, 1957).

[2] R. Seki and C. E. Wiegand, Annu. Rev. Nucl. Sci. 25, 241 (1975).

[3] J. Blomqvist, Nucl. Phys. B48, 95 (1972).

[4] H. Pilkuhn, Z. Phys. A276, 365 (1976).

[5] R. K. Cole, Jr., Phys. Lett. 25B, 178 (1967).

[6] E. B. Paul, *Nuclear and Particle Physics* (North-Holland, Amsterdam, 1969).

[7] For more detailed calculations see B. Fricke, Phys. Rev. Lett. 30, 119 (1973); J. L. Friar and J. W. Negele, Phys. Lett. 46B, 5 (1973).

[8] P. Vogel, At. Data Nucl. Data Tables 14, 599 (1974).

[9] George Rinker (private communication).

[10] M. Y. Chen, Y. Asano, S. C. Cheng, G. Dugan, E. Hu, L. Lidofsky, W. Patton, and C. S. Wu, Nucl. Phys. A254, 413 (1975).

[11] A. Zehnder, F. Boehm, W. Dey, R. Engfer, H. K. Walter, and J. L. Vuilleumier, Nucl. Phys. A254, 315 (1975).

[12] Z. Fried and A. D. Martin, Nuovo Cimento 29, 574 (1963).

[13] J. T. Routti and S. G. Prussin, Nucl. Instrum. Methods 72, 125 (1969).

[14] J. Kern, Nucl. Instrum. Methods 79, 233 (1970).

[15] B. L. Roberts, R. A. J. Riddle, and G. T. A. Squier, Nucl. Instrum. Methods 130, 559 (1975).

[16] M. Dojo, Nucl. Instrum. Methods 115, 425 (1974).

[17] G. Bertolini, F. Cappellani, and G. Restelli, Nucl. Instrum. Methods 112, 219 (1973).

[18] M. Leon and R. Seki, Phys. Rev. Lett. 32, 132 (1974). (a) R. J. Powers, in *Proceedings of International Topical Conference on Meson Nuclear Physics, Pittsburgh, 1976*, edited by P. D. Barnes, R. A. Eisenstein and L. S. Kisslinger (AIP, New York, 1976), p. 552.

[19] A. Buyrn, Nucl. Data Sheets 17, 97 (1976).

[20] B. L. Roberts, C. J. Batty, S. F. Biagi, M. Blecher, A. R. Kunselman, R. A. J. Riddle, J. D. Davies, G. J. Pyle, G. T. A. Squier, D. M. Asbury, and R. E. Haw-

kins, Bull. Am. Phys. Soc. 21, 586 (1976).

[21] R. Engfer, H. Schneuwly, J. L. Vuilleumier, H. K. Walter, and A. Zehnder, At. Data Nucl. Data Tables 14, 509 (1974).

[22] C. W. deJager, H. deVries, and C. deVries, At. Data Nucl. Data Tables 14, 479 (1974).

[23] M. Krell and T. E. O. Ericson, Nucl. Phys. B 11, 521 (1969).

[24] H. Koch and M. Sternheim, Phys. Rev. Lett. 28, 1061 (1972).

[25] P. D. Barnes, S. Dytman, R. A. Eisenstein, W. C. Lam, J. Miller, R. B. Sutton, D. A. Jenkins, R. J. Powers, M. Eckhause, J. R. Kane, B. L. Roberts, R. E. Welsh, A. R. Kunselman, R. P. Redwine, and R. E. Segel, Phys. Rev. Lett. 29, 1132 (1972).

[26] M. Alberg, E. M. Henley, and L. Wilets, Ann. Phys. (N.Y.) 96, 43 (1976).

[27] R. A. Bryan and R. J. N. Phillips, Nucl. Phys. B5, 201 (1968).

[28] T. E. Kalogeropoulos, in *High-Energy Physics and Nuclear Structure-1975, Proceedings of the Sixth International Conference, Santa Fe and Los Alamos*, edited by D. E. Nagle *et al.* (AIP, New York, 1975), p. 155.

[29] A. Deloff and J. Law, Phys. Rev. C 10, 2657 (1974); 11, 1067 (1975).

[30] K⁻ Collaboration, Nuovo Cimento 14, 315 (1959).

[31] K. Aslam and J. R. Rook, Nucl. Phys. B20, 159 (1970).

[32] C. B. Dover and S. H. Kahana (to be published).

[33] A. Deloff (to be published).

[34] H. Nishimura and T. Fujita, in Abstracts of Contributed Papers, Sixth International Conference on High Energy Physics and Nuclear Structure, Santa Fe, June 9–14, 1975, (unpublished), p. 174.

[35] W. M. Bugg, G. T. Condo, E. L. Hart, H. O. Cohn, and R. D. McCulloch, Phys. Rev. Lett. 31, 475 (1973); M. Leon and R. Seki, Phys. Lett. 48B, 173 (1974).

[36] W. J. Gerace, M. M. Sternheim, and J. F. Walker, Phys. Rev. Lett. 33, 508 (1974).

[37] The shifts of the 7 level for $\bar{p}Y$ and $\bar{p}Zr$ determined by the optical model analysis of the strong interaction effects were less than 1 eV, and in the direction which increases the difference between the proton and antiproton masses.

[38] A. Bamberger, U. Lynen, H. Piekarz, J. Piekarz, B. Povh, H. G. Ritter, G. Backenstoss, T. Bunaciu, J. Egger, W. D. Hamilton, and H. Koch, Phys. Lett. 33B, 233 (1970).

[39] B. L. Roberts (to be published).

[40] E. Hu, Y. Asano, M. Y. Chen, S. C. Cheng, G. Dugan, L. Lidofsky, W. Patton, C. S. Wu, V. Hughes, and D. Lu, Nucl. Phys. A254, 403 (1975).

[41] D. J. Horen, and M. B. Lewis, Nucl. Data Sheets 16, 25 (1975).

[42] T. E. O. Ericson and J. Hüfner, Nucl. Phys. B47, 205 (1972).

[43] C. E. Wiegand and G. L. Godfrey, Phys. Rev. A 9, 2282 (1974).

[44] G. Backenstoss, Annu. Rev. Nucl. Sci. 20, 467 (1970).